Energy & Environmental Science

PAPER

View Article Online
View Journal | View Issue

Cite this: *Energy Environ. Sci.*, 2016, **9**, 3448

A Gibeon meteorite yields a high-performance water oxidation electrocatalyst†

Florian Le Formal,[a] Néstor Guijarro,[a] Wiktor S. Bourée,[a] Aswin Gopakumar,[a] Mathieu S. Prévot,[a] Albert Daubry,[a] Loris Lombardo,[a] Charlotte Sornay,[a] Julie Voit,[a] Arnaud Magrez,[b] Paul J. Dyson[a] and Kevin Sivula*[a]

Received 15th August 2016,
Accepted 12th September 2016

DOI: 10.1039/c6ee02375d

www.rsc.org/ees

Examining the electrocatalytic performance of naturally-occurring metallic minerals is of interest for energy conversion applications given their unique atomic composition and formation history. Herein, we report the electrocatalytic function of an iron-based Gibeon meteorite for the oxygen evolution reaction (OER). After ageing under operational conditions in an alkaline electrolyte, an activity matching or possibly slightly superior to the best performing OER catalysts emerges, with stable overpotentials as low as 270 mV (for 10 mA cm^{-2}) and Tafel slopes of 37 mV $decade^{-1}$. The Faradaic efficiency for the OER was unity and no deterioration in performance was detected during 1000 hours of OER operation at 500 mA cm^{-2}. Mechanistic studies suggest an operando surface modification involving the formation of a 3D oxy(hydroxide) layer with a metal atom composition of $Co_{0.11}Fe_{0.33}Ni_{0.55}$, as indicated by Raman and XPS studies and trace Ir as indicated *via* elemental analysis. The growth of the catalyst layer was self-limiting to <200 nm after *ca.* 300 hours of operation as indicated through XPS depth profiling and cyclic voltammetry. The unique composition and structure of the Gibeon meteorite suggest that further investigation of Ir–Co–Ni–Fe systems or other alloys inspired by natural materials for water oxidation are of interest.

Broader context

The efficient and economical conversion of renewable electricity into the chemical energy of molecular bonds is particularly important for sustainable, carbon-neutral energy systems at a global scale. Indeed, routes for practical long-term energy storage and for the supply of industrial chemical feed-stocks are needed to replace dwindling fossil fuels. Molecular hydrogen (H_2) and methane (CH_4) are promising candidates for renewable fuels as they can be produced *via* the electrochemical reduction of water or CO_2, respectively, together with the associated oxidation reaction, which is most conveniently the electrochemical conversion of water into molecular oxygen (O_2). Robust, inexpensive, and highly effective electrocatalysts are thus needed to afford these reactions with low electrochemical overpotentials, and in recent years the search for highly active and earth-abundant catalysts has greatly intensified. While naturally-occurring materials have long been used as heterogeneous catalysts for many applications, few examples of natural minerals as electrocatalysts have emerged. In this work a naturally occurring material, the Gibeon meteorite, is investigated for its activity in the water oxidation reaction.

1. Introduction

The catalytic activity of naturally occurring minerals is both thought to have had a critical role in the origin of molecular diversity in prebiotic terrestrial chemistry (aiding the development of life itself)[1–5] and has been demonstrated to be important in many modern industrial applications.[6–13] For instance, Kaolinite (a common layered silicate clay) has been shown to catalyze the partial hydrolysis of molybdenum sulfate (which is present in deep-sea sediments and regulates the redox state of oceans),[3] and has been suggested in the prebiotic synthesis of oligopeptides from α-amino acids.[14] Zeolites found in volcanogenic sedimentary rocks have been shown to exhibit catalytic activity towards the degradation of pollutants in wastewater and the conversion of hydrocarbons.[6] Natural forms of iron oxyhydroxides (*e.g.* ferrihydrites) have been particularly scrutinized both as oxidants for water pollutants involving Fenton-type chemistry[7,8] and as potential drivers of water photolysis that depleted surface moisture on Mars.[4] Other naturally occurring minerals, including sphalerite,[9] georgeite[10] and dolomite,[11] have been reported to enhance the rates of diverse chemical reactions such as biomass conversion, polymerization of styrene or dye degradation.[11–13] Despite their promising activity,

[a] *Institute of Chemical Sciences and Engineering (ISIC), Ecole Polytechnique Fédérale de Lausanne (EPFL), 1015-Lausanne, Switzerland. E-mail: kevin.sivula@epfl.ch*
[b] *Institute of Physics (IPHYS), Ecole Polytechnique Fédérale de Lausanne (EPFL), 1015-Lausanne, Switzerland*

† Electronic supplementary information (ESI) available: Fig. S1–S7 and Table S1 as described in the main text. See DOI: 10.1039/c6ee02375d

naturally-occurring minerals have not been deeply considered as electrocatalysts as, typically, their oxidized form results in poor electronic conductivity rendering them ill-suited as electrodes. However, electronic potential gradients between adjacent crystallographic surfaces or disparate chemical phases have been shown to be important to promote reactivity and drive electronic charge transport in naturally occurring minerals.[4,15] This feature inspires a search for naturally-occurring functional electrocatalysts. One class of mineral, meteoric iron, retains its electrical conductivity and is thus a compelling candidate to demonstrate the novel electrocatalytic activity of a naturally occurring mineral.

Meteoric iron originates from fragments of large ancient asteroid cores, which after being shattered by collisions, survived passage through the Earth's atmosphere and impact with the Earth's surface.[16] Due to their high density and prevalence, iron meteorites account for *ca.* 90% of the mass of all known terrestrial meteorites, about 500 tons.[17] The Gibeon meteorite, in particular, has the largest strewnfield known with pieces discovered over 20 000 km^2 in Namibia and a total collected mass exceeding 21 tons.[18] This meteorite is reported to be mainly composed of iron and nickel, with lower amount of cobalt and phosphorus as well as traces of iridium, germanium and gallium.[18,19] Mineralogically, it belongs to the class of fine octahedrites (group IVA), typically with three different finely intermixed phases: Kamacite (ferrite phase, Ni poor), Taenite (austenite phase, Ni rich) and Plessite (a mixture of Kamacite and Taenite).[20,21] In addition, Widmanstätten patterns are typically present indicating that the meteorite underwent crystal phase formation at remarkably slow cooling rates (*ca.* 50 K in 10^6 years).[22,23] The unique formation conditions and crystallographic structure of the Gibeon meteorite have been thoroughly investigated especially with regards to the orientational relationship between the separate phases,[21,24–29] and its distinctive magnetic properties.[30] Despite these studies, neither this material, nor any other meteorite to the best of our knowledge, has been investigated for its (electro)catalytic properties. Indeed their composition suggests possible activity in the water oxidation reaction,[31] a kinetically challenging reaction that requires large overpotentials. Moreover, the exceptional thermal history, crystal structure and remarkable atomic composition of the Gibeon meteorite provide a unique opportunity for study.

2. Experimental section

2.1. Electrode preparation

The Gibeon pieces were cut into approximately 0.5 mm thick slices (1 cm × 2 cm). The samples were then polished to a mirror-like finish with a 30 μm lapping film (3 M), and soldered to an electrical lead (Cu wire). The surface was rinsed with ethanol and deionized water (MilliQ, 18.2 MΩ cm^{-1}), then fixed to a glass support with epoxy. The geometric surface area was defined by covering the inactive surface with corrosion-resistant epoxy (Araldite 2000, 2014-1), as shown in Fig. 1a. The active area was kept between 0.3 and 0.6 cm^2. Multiple electrodes were tested using an identical preparation procedure and originated from the same sample of the meteorite which was approximately 100 × 100 × 70 mm^3 (see Fig. S1, ESI†).

2.2. Electrochemical characterization and operation

The electrodes were treated and tested in a three-electrode set-up (BioLogic SP-200 potentiostat), with a Pt counter electrode and

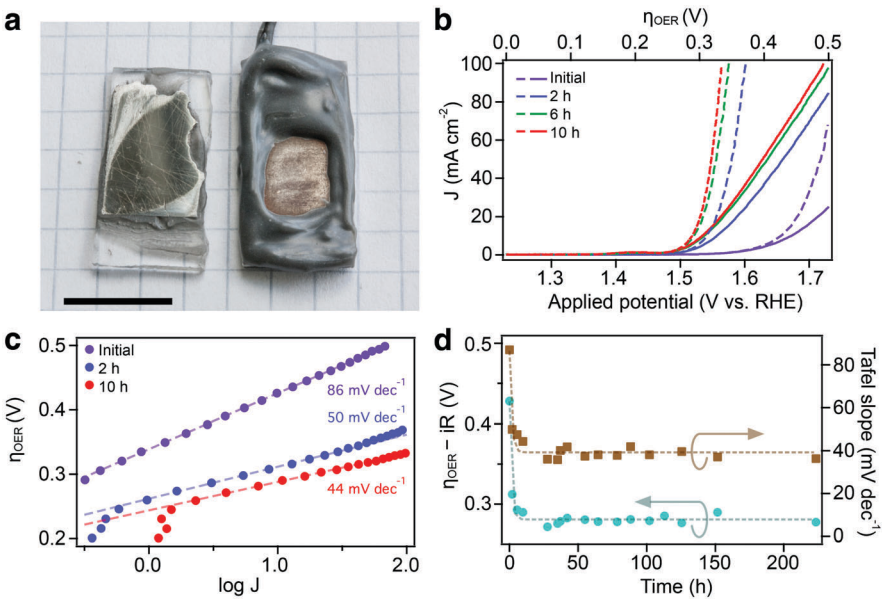

Fig. 1 (a) Photographs of Gibeon meteorite pieces, (left) after cutting and cleaning and (right) after OER operation (scale bar: 1 cm). In the right sample, the active area is defined by the Gibeon surface not recovered with epoxy. (b) Current density *versus* applied voltage, without and with *iR* drop correction (plain and broken lines respectively) for the Gibeon sample before and during water oxidation at 500 mA cm^{-2}. (c) Tafel analysis before (purple), and after 2 (blue) and 10 (red) hours of oxidation; linear fits are shown in broken lines. (d) Summary of the change in overpotential measured at 10 mA cm^{-2} (cyan, left axis) and Tafel slope (brown, right axis) with oxidation time.

an Ag/AgCl KCl(sat) reference electrode. The electrolyte was a 1 M NaOH solution in deionized water (measured pH 13.4). The electrodes were immersed so that the active area was in full contact with the electrolyte. The potentials are referenced against the reversible hydrogen electrode (RHE), calculated according to *E vs.* RHE = *E vs.* Ag/AgCl + $E^0_{Ag/AgCl}$ + 0.0591 × pH with *E vs.* Ag/AgCl as the potential applied *versus* Ag/AgCl and $E^0_{Ag/AgCl}$ as the standard potential of the silver/silver chloride electrode against the standard hydrogen electrode (+0.197 V in saturated KCl). The overpotential corresponds to the potential difference between the applied potential against RHE and the standard potential of water oxidation (1.23 V *vs.* RHE). The reference electrode was removed from the experimental setup after performance tests (CV and LSV) to reduce the diffusion of chlorine ions to the electrolyte during ageing. Sample ageing was performed by maintaining a constant anodic current density of 500 mA cm^{-2} between the working and the counter electrodes. Linear sweep voltammetry, between 1.0 V *vs.* RHE and 1.8 V *vs.* RHE, was used to characterize the sample activity periodically during ageing with a sweep rate of 10 mV s^{-1}. Potential corrections for the *iR* drop were applied using the series resistance obtained from impedance spectroscopy performed before operation at 1.0, 1.1, 1.2, 1.3 and 1.4 V *vs.* RHE at a frequency between 1 Hz and 10^5 Hz (perturbation amplitude of 10 mV). The intercept with the bottom axis in a Nyquist plot at a high frequency (series resistance) was used as the uncompensated resistance for *iR* correction (usually between 3 and 4 Ohms). Tafel slopes were estimated from the LSV performed at a slow scan rate (10 mV s^{-1}), similar to other reports.[32,33] Cyclic voltammograms (CVs) were also recorded periodically during ageing between 0.6 and 1.5 V *vs.* RHE at a scan rate of 10 mV s^{-1}. No *iR* correction was performed on the analysis of the CV data. The Faradaic efficiency was measured for a Gibeon electrode, initially and after 5 hours of operation at 500 mA cm^{-2} in 1 M NaOH at a constant current density of 10 mA cm^{-2}. The gas chromatograph (GC) was calibrated with an electrochemical cell containing two platinum foils as the working and counter electrodes (assuming 100% Faradaic efficiency for this setup). The integrated area of the O_2 signal during measurement of the steady-state chronopotentiometry was determined to be 2.68 ± 0.02 and 2.61 ± 0.02 (initially and after 5 hours respectively), which differ by 3% and 1% to the Faradaic efficiency of 100% obtained from the calibration (±5% error).

2.3. Spectroscopic analysis

The chemical composition of the Gibeon meteorite was determined using a Shimadzu 9000 ICP-OES system. A small fraction (1 g) of the Gibeon was digested in aqua-regia prior to analysis. Calibration standards were analyzed and cross-checked with commercially purchased spectroscopic standard solutions. The measurements were operated at 45 kV and 40 mA in a continuous mode with a scanning rate of 0.01° min^{-1} in the 2θ range between 20° and 90°. Raman spectra were obtained on a confocal Raman microscope XploRa Plus (Horiba), where the excitation line was provided by an Nd:YAG (doubled) laser (532 nm). XPS spectra were acquired using a KRATOS AXIS ULTRA spectrometer (Al Kα source, 600 × 750 μm spot size). The binding energy scale was calibrated from the hydrocarbon contamination using the C1s peak at 284.8 eV. Pass energies of 187.85 eV (step: 0.8 eV) and 46.95 eV (step: 0.2 eV) were used for the XPS surveys and multiplex measurements respectively. Major peaks are assigned according to the handbook of X-ray Photoelectron Spectroscopy by Moulder *et al.*[34] XPS peaks were fitted to extract the relative amount of each species using the PHI Multipack software. Samples were etched with Ar^+ ions at a rate of 8.8 nm min^{-1} and the surface composition was recorded at regular intervals. HR-SEM images were recorded using a Zeiss Merlin microscope.

2.4. Diffraction techniques

Powder XRD patterns of the Gibeon meteorite before operation were obtained using a PANalytical Empyrean XRD with Bragg-Brentano geometry fitted with a PANalytical PIXcel-1D detector using Ni filtered Cu-Kα radiation (λ = 1.54056 Å).

3. Results and discussion

A portion of the Gibeon meteorite (see photograph in Fig. S1, ESI†) was first pulverized for elemental characterization using inductively coupled plasma optical emission spectrometry (ICP-OES). The main elements were found to be Fe (93.8%), Ni (5.5%), Co (0.4%) and P (0.2%) with traces of Ga, Ge, and Ir. The measured composition is comparable to analyses presented by Buchwald *et al.*[18] with a slightly lower nickel content compared to previous reports (5.5% *vs.* 7.8–8%, see Table S1 in the ESI†). This difference suggests that the sample is mostly composed of the Kamacite phase. Indeed, XRD analysis (Fig. S2 in the ESI†) revealed diffraction peaks in agreement with the Kamacite BCC crystal structure (space group $Im\bar{3}m$) and a unit cell side length of 2.87 Å.

3.1. OER performance

To assess the electrocatalytic performance, the Gibeon sample was cut into slices with thicknesses of *ca.* 0.5 mm, and was cleaned and polished before fixing on a glass support, attaching an electrical lead, and sealing with epoxy. A photograph of a prepared electrode before sealing and after electrochemical testing is shown in Fig. 1a. The electrochemical behaviour of a Gibeon electrode in an alkaline electrolyte is shown in Fig. 1b–d. The as-measured and *iR*-corrected linear-scanning voltammograms (LSVs) are shown in Fig. 1b with respect to the applied potential, with the initial test of the Gibeon electrode showing an increase of anodic current when the potential exceeds +1.6 V *vs.* the reversible hydrogen electrode (RHE), suggesting catalytic activity towards the oxygen evolution reaction (OER). The overpotential relative to the OER standard potential of 1.23 V *vs.* RHE is also shown on the top axis of Fig. 1b. To assess the stability of the Gibeon electrode and to characterize the evolution of the OER performance with ageing, the electrodes were maintained at a current density commonly used in alkaline electrolyzers (500 mA cm^{-2}) for extended duration. The catalytic performance

was quantified periodically by LSV. As figures of merit, we used the overpotential for the OER (η_{OER}) required to extract 10 mA cm^{-2} from the electrode (as defined by McCrory *et al.*[31]) and the estimated Tafel slopes which are shown with respect to the ageing time at 500 mA cm^{-2} in Fig. 1d. The Tafel behavior (Fig. 1c) is linear over two orders of magnitude in the current density validating the use of the Tafel analysis.

A significant positive effect is evident upon operating the Gibeon electrode at a high current density. The η_{OER} dropped rapidly from 0.43 to 0.30 V, and the Tafel slope decreased from 86 to 44 mV decade^{-1} after 10 hours of operation. This improvement with ageing stabilized to give a consistent performance after *ca.* 25 hours. The lowest η_{OER} obtained with a Gibeon electrode was 0.27 V with a Tafel slope of 37 mV decade^{-1}. We note that the improvement upon ageing was reproducible over 5 samples tested under identical conditions (average η_{OER} of 0.31 V and Tafel slope of 38 mV decade^{-1} after 20 hours of ageing) and the electrodes were stable for at least 1000 hours (see the ESI,† Fig. S3), which was the longest duration an electrode was tested.

3.2. Quantification of active species

In addition to the significantly improved η_{OER} and Tafel slope upon ageing, a reversible redox wave, detectable using cyclic voltammograms (CVs), was found to develop during prolonged electrode operation at a high current density. CVs taken periodically during the ageing process are shown in Fig. 2a. The oxidation (*ca.* +1.4 V *vs.* RHE) and reduction (*ca.* +1.3 V *vs.* RHE) potentials of the redox wave were found to correspond well with the $Ni^{2+/3+}$ redox couple in the alkaline electrolyte.[32,35,36] The potential of the $Ni^{2+/3+}$ couple is also noted to shift its position with ageing. Indeed, both the detection of the $Ni^{2+/3+}$ redox wave and its position in synthetically-prepared iron–nickel based electrode systems have been reported to be dependent on the Ni : Fe atomic stoichiometry.[32,33,35,37] In the case of the Gibeon electrodes, the redox wave shifts toward more negative potentials with ageing and the magnitude of the wave increases, suggesting that both the relative (compared to Fe) and absolute surface concentration of the Ni atoms increases. Moreover, both the anodic and cathodic peak potentials show a linear correlation with η_{OER} (see the ESI,† Fig. S4), which further suggests a direct relationship between the formation of a nickel-based surface species and the improved OER catalysis.

The magnitude of the $Ni^{2+/3+}$ redox wave was next quantified to estimate the surface concentration of catalytically-active species by integration with the scan rate to give the number of electrochemically-accessible nickel sites.[35,37] The surface charge density with respect to the geometric electrode area is shown against the ageing time in Fig. 2b. Interestingly, the η_{OER} reached a stable value only after *ca.* 10 hours of operation, whereas the density of active sites is shown to stabilize after 300 hours to $\sim 30 \times 10^{16}$ cm^{-2}. These results show that (i) the saturation of η_{OER} occurs for a certain density of catalytic sites and (ii) that a portion of the current recorded in the LSV after 10 hours could be attributed to the surface modification process concomitant to the OER. However, the Faradaic efficiency

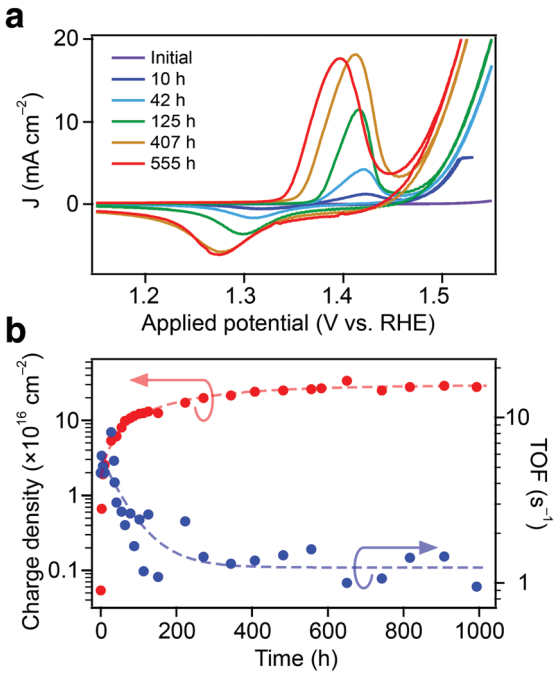

Fig. 2 (a) Examples of cyclic voltammograms of a Gibeon electrode measured at 10 mV s^{-1} after different oxidation periods in 1 M NaOH. (b) Charge density quantified under the reduction peak appearing in cyclic voltammograms and the turn-over frequencies (TOF) against operation time at 500 mA cm^{-2} (dotted lines: logistic function fits).

towards oxygen evolution measured at 10 mA cm^{-2} on a Gibeon electrode before ageing and after 5 hours of operation was found to be 100% within a 5% measurement error in both cases (see the Methods section). This indicates that the electron current associated with the surface modification is negligible compared to the OER at 10 mA cm^{-2}.

3.3. Turn-over frequencies

Catalytic turn-over frequencies (TOFs) were also estimated at an applied overpotential of 0.3 V according to the number of active centers detected *via* CV (accounting 1 e$^-$ per active species and 4 e$^-$ per O_2 molecule produced). The estimated TOF with respect to the ageing time is also shown in Fig. 2b. In the first few hours of oxidation a TOF value up to 5 s^{-1} is found, which exceeds the best results recorded by Trotochaud *et al.* (1–2 s^{-1}) using the same approach with electrodeposited $Ni_{1-x}Fe_xOOH$ catalyst layers.[35] After operation for *ca.* 100 hours the TOF settles to values similar to the state-of-the-art. Indeed, the high TOF reported initially is likely overestimated due to the participation of other metallic atoms (Fe, Co) in the oxygen evolution catalysis, which is not considered in this analysis. Conversely, lower values obtained by Qiu *et al.* (0.1 s^{-1}), for a synthetic NiFe catalyst exhibiting similar η_{OER}, may be due to the overestimation of the catalytic center density in that film, as all metallic atoms were considered.[33]

3.4. Spectroscopic analyses

As the stabilized density of catalytically active sites per geometric surface area based on the nickel redox couple (equivalent to 30 sites Å^{-2}) is greater than the density of atoms on the surface

planes of the Kamacite BCC crystal structure, a change in surface morphology (*e.g.* the formation of nanostructures) seems likely. However, the formation of a significantly roughened surface was not observed upon examination with high-resolution electron microscopy both before and after the ageing process (see SEM, Fig. 3a and b).

Nonetheless, the appearance of fissures on the surface of the aged electrode suggests the formation of a hydrated gel layer that contracts when the electrode is dried and placed under vacuum for SEM analysis. The formation of a catalytically active 3D hydrous layer *via* metal electrode anodization has been described previously.[38] Further insights into the chemical nature of this emergent layer on the Gibeon electrode is given using Raman spectroscopy. Spectra before and after electrochemical operation are shown in Fig. 3c. Two main peaks are detected at 550 and 675 cm^{-1} in the pristine sample. These peaks match the Raman response from the oxidized iron species: Fe_3O_4 (550 and 670–675 cm^{-1}), γ-Fe_2O_3 (650–740 cm^{-1}) and γ-FeOOH (660 cm^{-1}).[39,40] After 48 hours of OER operation, additional peaks appear in the spectrum, *i.e.* a band between 294 and 350 cm^{-1}, one feature including two peaks at 480 and 527 cm^{-1} and a broad band centered at 1390 cm^{-1}. The two first peaks are likely related to the increase in oxidized iron species on the surface as Fe_3O_4 (292 cm^{-1}), α-Fe_2O_3 (290–350 cm^{-1}) and γ-FeOOH (243–300 cm^{-1}) have shown a response at these wavenumbers.[40,41] The second feature (480–527 cm^{-1}) is attributable to defective or disordered $Ni(OH)_2$. Both the α and β forms exhibit Ni–O bands in the range of 445–465 cm^{-1}, which are shifted positively when $Ni(OH)_2$ is disordered, doped or alloyed with Fe, and characteristic peaks have been detected at 530 and 526 cm^{-1}.[32,42,43] It should be noted that cobalt(III) species respond in the 480–527 region as well. The principle peaks of CoOOH, $Co(OH)_2$ and Co_3O_4 are found at 503 cm^{-1}, 523 cm^{-1} and 481 cm^{-1}, respectively.[44,45] The broad feature centered at 1390 cm^{-1} is located in the range characteristic of lattice OH vibrations in the hydroxide layers and can be attributed to the superposition of the Fe–OH and Ni–OH responses, which have been detected at 1335 and around 1400 cm^{-1} for $Fe(OH)_3$ and α-$Ni(OH)_2$, respectively.[41,46] Overall, the Raman experiments confirm the formation of (oxy)hydroxides of iron and nickel and are also consistent with cobalt species at the surface of the Gibeon electrode after ageing.

X-ray photoelectron spectroscopy (XPS) surface and depth profiling were used to gain further insight into the nature and extent of the 3D catalyst layer. The XPS survey of the Gibeon electrode surface before and after operation shows the presence of carbon, oxygen, iron, nickel and a small amount of cobalt (see the ESI,† Fig. S5), and the atomic composition was obtained at different depths inside the material after etching the surface with Ar^+ ions. The atomic profiles obtained for the electrode before operation and after 50 hours at 500 mA cm^{-2} are compared in Fig. 4.

The presence of adventitious carbon was noted on the surface of both electrodes. For the pristine electrode, the iron content increases relatively rapidly with depth to 80 at% and the oxygen content decreases from *ca.* 30 at% at the surface to below detectable limits over the same length scale. XPS detected Ni in the pristine sample at 3.7 ± 1.4 at% on average over the 250 nm tested, these results are consistent with the *ca.* 5 at% Nickel detected when using ICP-OES. In contrast in the aged electrode, Ni rose to over 20 at% and oxygen also increased in the

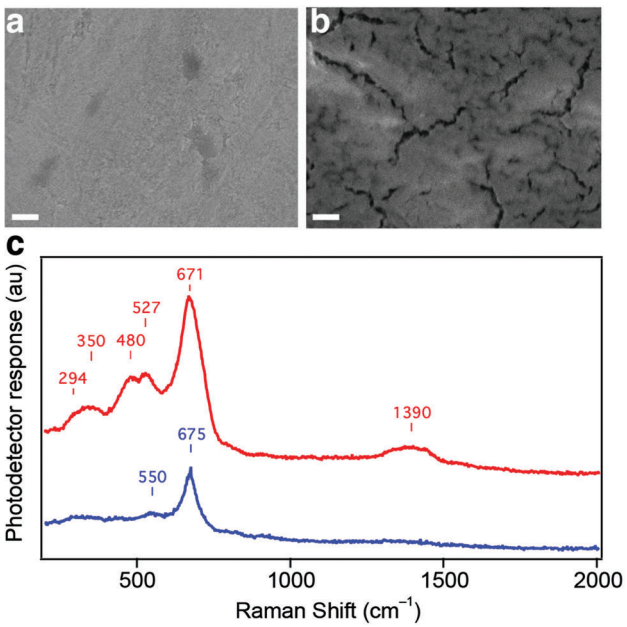

Fig. 3 Scanning electron micrographs of a Gibeon electrode before (a) and after (b) 50 hours of operation at 500 mA cm^{-2} in 1 M NaOH (scale bars 200 nm) and (c) Raman spectra of a Gibeon sample before (blue) and after 48 hours of oxidation (red). Raman shift positions of the detected peaks are overlaid on the graph.

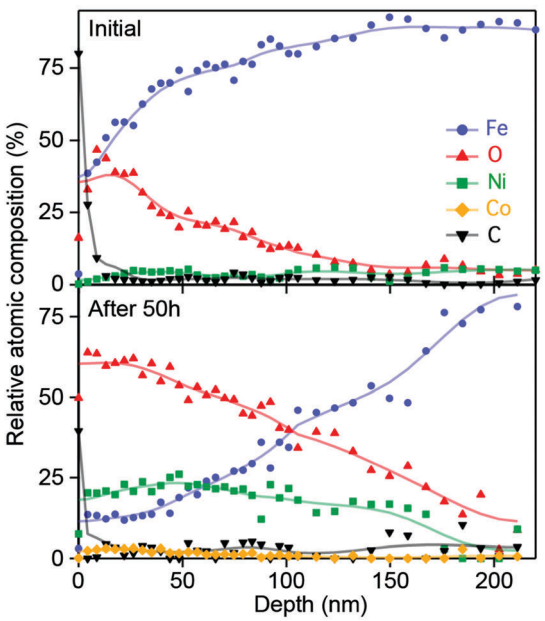

Fig. 4 Atomic composition profile obtained *via* XPS of a Gibeon sample before (top) and after 50 hours of operation at 500 mA cm^{-2} in a 1 M NaOH electrolyte (bottom). Spectra were obtained for both samples at different times after etching the surface with Ar^+ ions at a rate of 8.8 nm min^{-1}.

first 100 nm depth of the film, whereas the iron fraction was reduced to 12 at% at the surface of the oxidized electrode, rising to reach bulk concentrations after 200 nm in depth. Cobalt was detected in the pristine sample, but not at a statistically significant concentration considering the uncertainty of the XPS measurement. However, in the aged electrode, Co was detected at an atomic ratio slightly exceeding 5 at% near the surface, with the concentration decreasing to background levels at a depth of 150 nm. The gradient of oxygen concentration implies a change in the oxidation state of the metal atoms through the depth of the film. The oxidation states of Fe, Ni and the trace Co were investigated by examining their characteristic $2p_{3/2}$ peak (Fig. S6 and S7, ESI†) at several depths inside the electrode. In the pristine electrode, both iron and nickel were detected at binding energies close to those associated with their metallic state Fe^0 and Ni^0, whereas the Co response was not visible due to the strong response of the iron Auger Line (L3M45M45). After 50 hours of operation, the nickel peak shifted from 853 to 857 eV, characteristic of the Ni^{2+} state (particularly for amorphous $Ni(OH)_2$).[47] Similarly, the Fe peak also shifted to higher binding energies (706 to 711.7 eV), which can be assigned to the ferric (3+) state as detected in FeOOH.[48] For cobalt in the aged electrode, the $2p_{3/2}$ signal was detected at 780.3 eV (as measured in CoOOH or Co_2O_3).[34] After 20 minutes of etching (176 nm) the aged electrode, the signals return to the metallic states detected for the pristine electrode, indicating that only the surface layer is modified. Overall, the composition and oxidation state characterization using XPS suggests that the 3D catalyst layer on the aged electrode has a metal cation surface stoichiometry of $Co_{0.11}{}^{3+}Fe_{0.33}{}^{3+}Ni_{0.55}{}^{2+}$ with a smooth gradient toward more reduced states over 200 nm towards the bulk concentrations. It should be noted that while the XPS measurements indicate that nickel is primarily in the 2+ oxidation state, during OER operation the 3+ oxidation state is present in the active catalyst as the potential applied is positive of the $Ni^{2+/3+}$ redox wave. Fe^{4+} is also likely present in the catalyst under operation.[49] The metal composition of the active layer is likely related to the initial composition of the meteorite and to the experimental conditions used for OER operation. The influence of these parameters will be the focus of future investigations.

3.5. Discussion

The Gibeon meteorite can be processed to form a highly-active 3D electrocatalyst for the OER reaction. The procedure requires cutting, polishing and ageing of the resulting electrode by driving the OER at 500 mA cm^{-2}. The mechanism for the formation of the catalysts is consistent with the selective etching of iron atoms from the surface with concurrent concentrations of Ni and Co in the active layer, which is supported by the observation of a black deposit on the counter electrode during the initial stages of catalyst formation from the reduction of the etched iron. This type of formation mechanism has been discussed in more detail in a previous study using stainless steel.[37] Previous investigations of synthetic nickel–iron catalysts have suggested the formation of a layered double hydroxide (brucite structure) under operation,[50,51] which is characterized by the transformation of $Ni(OH)_2$ to NiOOH at potentials anodic of 1.4 V *vs.* RHE. Such a crystallographic arrangement with layers of nickel (oxy)hydroxide, separated by water and hydroxyl ions, is highly porous and enables a greater amount of catalyst species to be in contact with the electrolyte. This mechanism is consistent with our observation of the increase of the $Ni^{2+/3+}$ redox wave intensity with the ageing time. The extensive ageing test performed in this work shows that the formation of the active catalyst layer is self-limiting as the magnitude of the Ni redox wave stabilizes after *ca.* 300 hours.

In addition to the formation of an (oxy)hydroxide layer, the unique composition of the Gibeon meteorite may be important for an outstanding performance. Indeed, the η_{OER} and Tafel behavior of this catalyst are equivalent to, or even slightly better than, state-of-the-art manufactured NiFe electrocatalysts (which show $\eta_{OER} \sim 0.28$–0.35 V at 10 mA cm^{-2} and Tafel slopes in the range of 30–40 mV $decade^{-1}$),[33,52–54] and IrO_2 and RuO_2, two benchmark OERs (also with $\eta_{OER} \sim 0.28$–0.32 V and a small Tafel slope of 30–40 mV dec^{-1}).[31,55]

In previous work on NiFe electrocatalysts, the Ni : Fe ratio has been shown to impact the catalytic performance by affecting the electronic conductivity, thereby modifying the local electronics of active Ni centers.[32,35,56,57] These studies have established a correlation between the Ni:Fe atomic stoichiometry and the appearance of the $Ni^{2+/3+}$ redox wave, which provides further insight into the composition of the active Gibeon catalyst. Specifically, both the anodic and cathodic waves from $Ni^{2+/3+}$ were reported to be only observable for a Ni : Fe ratio >69 at%. However, the results obtained with a Gibeon electrode differ from these previous studies as we observe the appearance of both oxidation and reduction waves after ageing for only 15 minutes when the surface analysis only suggests the Ni : Fe ratio is <60 at% after 50 hours. This discrepancy suggests that surface Co atoms may also be important for the appearance of the redox wave in the CV. Nonetheless, based on the uncertainty with the redox wave assignment of the catalyst composition, the XPS-based composition is more reliable. In addition to the concentration of Ni and Co in the catalyst layer, the possible role of other trace elements (Ga, Ge and Ir) on the high activity cannot be discounted despite their concentration being below the quantification limit for XPS. In particular, IrO_2 is known to be a state-of-the-art OER catalyst.[31]

While the atomic composition is undoubtedly important for the high activity, the native atomic arrangements in the Kamacite crystal structure and the unique thermal history of the Gibeon meteorite are not likely to be important factors in the high OER electrocatalytic activity. Indeed, the initial performance of the Gibeon electrode was unremarkable. Only after the formation of the 3D (oxy)hydroxide layer with concentrated Ni and Co—which destroys the crystallinity of the electrode—was the state-of-the-art catalytic activity recorded. Despite this, overall our study of the electrocatalytic behaviour of the Gibeon meteorite has suggested that further investigation of Ir–Co–Ni–Fe based OER electrocatalysts is warranted to better understand possible synergistic effects and, moreover, indicated for the first time that naturally-occurring materials can function as state-of-the-art electrocatalysts.

4. Conclusions

We have shown the robust and exceptional electrocatalytic activity of a natural mineral of extraterrestrial origin, *i.e.* a Gibeon meteorite. Electrodes prepared from this iron-based mineral exhibited a state-of-the-art performance for the oxygen evolution reaction in the alkaline electrolyte with an overpotential as low as 0.27 V for a current density of 10 mA cm^{-2} and a Tafel slope of 37 mV $decade^{-1}$, comparable to the top-performing synthetic Fe–Ni catalysts. The catalytic activity of the Gibeon electrodes emerged after 10 hours of operation at 500 mA cm^{-2} due to the etching of iron and the formation of a 3D oxy(hydroxide) layer with a metal atom composition of primarily $Co_{0.11}Fe_{0.33}Ni_{0.55}$, as indicated from the Raman and XPS studies, and trace Ir as indicated from the elemental analysis. The growth of the catalyst layer was self-limiting to a depth of <200 nm after *ca.* 300 hours of operation as indicated from the depth profiling and CV results, and showed stability for at least 1000 hours. While the crystal structure of the Gibeon meteorite likely does not contribute to the electrocatalytic activity due to the atomic rearrangement implied, its unique composition suggests that further investigation of the Ir–Co–Ni–Fe systems for water oxidation is of interest. Finally, this study demonstrated the ability of natural materials to be highly active as electrocatalysts and potentially in other catalytic processes.

Author contributions

P. J. D. and K. S. conceived the project and supervised the work. F. L. F. and K. S. designed the experiments. F. L. F. prepared the electrodes and performed the electrochemical measurements. A. D., L. L., C. S. and J. V. performed the initial electrocatalytic evaluation. N. G. measured the faradaic efficiencies and discussed the XPS data. W. S. B. performed Raman spectroscopy. A. G. performed the elemental analysis. M. S. P. performed scanning electron microscopy. A. M. performed the XRD measurements. K. S. and F. L. F. prepared the figures and wrote the manuscript. The subsequent editing/improvement was performed by K. S., P. J. D., N. G., F. L. F., W. S. B. and M. S. P.

Acknowledgements

The authors would like to thank Y. Morier for precision slicing of the Gibeon meteorite sample, Dr P. Mettraux (CIME, EPFL) for measurement and discussion of the XPS data, and X. Yu for helpful discussion of the XPS data. The Swiss Competence Centers for Energy Research (SCCER Heat and Electricity Storage, contract # KTI.2014.0113) is gratefully acknowledged for the financial support.

Notes and references

1 H. J. Cleaves II, A. M. Scott, F. C. Hill, J. Leszczynski, N. Sahai and R. Hazen, *Chem. Soc. Rev.*, 2012, **41**, 5502–5525.
2 M. F. Hochella, S. K. Lower, P. A. Maurice, R. L. Penn, N. Sahai, D. L. Sparks and B. S. Twining, *Science*, 2008, **319**, 1631–1635.
3 T. P. Vorlicek and G. R. Helz, *Geochim. Cosmochim. Acta*, 2002, **66**, 3679–3692.
4 C. M. Eggleston, J. R. Stern, T. M. Strellis and B. A. Parkinson, *Am. Mineral.*, 2012, **97**, 1804–1807.
5 M. Rao, D. G. Odom and J. Oró, *J. Mol. Evol.*, 1980, **15**, 317–331.
6 F. A. Mumpton, *Proc. Natl. Acad. Sci. U. S. A.*, 1999, **96**, 3463–3470.
7 W. P. Kwan and B. M. Voelker, *Environ. Sci. Technol.*, 2003, **37**, 1150–1158.
8 J. Filip, R. Zboril, O. Schneeweiss, J. Zeman, M. Cernik, P. Kvapil and M. Otyepka, *Environ. Sci. Technol.*, 2007, **41**, 4367–4374.
9 Y. Chen, A. Lu, Y. Li, L. Zhang, H. Y. Yip, H. Zhao, T. An and P.-K. Wong, *Environ. Sci. Technol.*, 2011, **45**, 5689–5695.
10 S. A. Kondrat, P. J. Smith, P. P. Wells, P. A. Chater, J. H. Carter, D. J. Morgan, E. M. Fiordaliso, J. B. Wagner, T. E. Davies, L. Lu, J. K. Bartley, S. H. Taylor, M. S. Spencer, C. J. Kiely, G. J. Kelly, C. W. Park, M. J. Rosseinsky and G. J. Hutchings, *Nature*, 2016, **531**, 83–87.
11 S. Rapagnà, *Biomass Bioenergy*, 2000, **19**, 187–197.
12 D. H. Solomon and M. J. Rosser, *J. Appl. Polym. Sci.*, 1965, **9**, 1261–1271.
13 Y. Dong, K. He, B. Zhao, Y. Yin, L. Yin and A. Zhang, *Catal. Commun.*, 2007, **8**, 1599–1603.
14 K. I. Zamaraev, V. N. Romannikov, R. I. Salganik, W. A. Wlassoff and V. V. Khramtsov, *Origins Life Evol. Biospheres*, 1997, **27**, 325–337.
15 S. V. Yanina and K. M. Rosso, *Science*, 2008, **320**, 218–222.
16 M. K. Weisberg, T. J. McCoy and A. N. Krot, in *Meteorites and the Early Solar System II*, ed. D. S. Lauretta and H. Y. McSween, 2006, pp. 19–52.
17 D. J. Darling, *The Universal Book of Astronomy: From the Andromeda Galaxy to the Zone of Avoidance*, Wiley, 2003.
18 V. F. Buchwald, *Handbook of Iron Meteorites: Their History, Distribution, Composition and Structure. Iron meteorites*, University of California Press, 1975.
19 F. Hasan and H. J. Axon, *J. Mater. Sci.*, 1985, **20**, 590–596.
20 P. Parz, M. Leitner, W. Sprengel, H. Reingruber and W. Puff, *J. Phys.: Conf. Ser.*, 2013, **443**, 12032.
21 W. Weiss and H. J. Bunge, *J. Appl. Crystallogr.*, 2001, **34**, 566–572.
22 Y. He, S. Godet, P. J. Jacques and J. J. Jonas, *Acta Mater.*, 2006, **54**, 1323–1334.
23 M. Weller and U. G. K. Wegst, *Mater. Sci. Eng., A*, 2009, **521–522**, 39–42.
24 S. Höfler, W. Schäfer and G. Will, *Phys. B*, 1989, **156–157**, 675–677.
25 H. J. Bunge, W. Weiss, H. Klein, L. Wcislak, U. Garbe and J. R. Schneider, *J. Appl. Crystallogr.*, 2003, **36**, 137–140.
26 M. Kotsugi, T. Wakita, T. Taniuchi, K. Ono, M. Suzuki, N. Kawamura, M. Takagaki, M. Taniguchi, K. Kobayashi, M. Oshima, N. Ishimatsu and H. Maruyama, *e-J. Surf. Sci. Nanotechnol.*, 2006, **4**, 490–493.
27 B. Hutchinson and J. Hagström, *Metall. Mater. Trans. A*, 2006, **37**, 1811–1818.

28 G. Nolze and V. Geist, *Cryst. Res. Technol.*, 2004, **39**, 343–352.
29 Y. L. He, S. Godet, P. J. Jacques and J. J. Jonas, *Solid State Phenom.*, 2005, **105**, 121–126.
30 M. Kotsugi, F. Z. Guo, M. Taniguchi, N. Ishimatsu and H. Maruyama, *Surf. Sci.*, 2007, **601**, 4326–4328.
31 C. C. L. McCrory, S. Jung, I. M. Ferrer, S. M. Chatman, J. C. Peters and T. F. Jaramillo, *J. Am. Chem. Soc.*, 2015, **137**, 4347–4357.
32 M. W. Louie and A. T. Bell, *J. Am. Chem. Soc.*, 2013, **135**, 12329–12337.
33 Y. Qiu, L. Xin and W. Li, *Langmuir*, 2014, **30**, 7893–7901.
34 J. F. Moulder and J. Chastain, in *Handbook of X-ray photoelectron spectroscopy: a reference book of standard spectra for identification and interpretation of XPS data*, ed. J. F. Moulder and J. Chastain, Perkin-Elmer Corporation, Eden Prairie, Minn, update, 1992.
35 L. Trotochaud, S. L. Young, J. K. Ranney and S. W. Boettcher, *J. Am. Chem. Soc.*, 2014, **136**, 6744–6753.
36 M. E. G. Lyons and M. P. Brandon, *Int. J. Electrochem. Sci.*, 2008, **3**, 1386–1424.
37 H. Schäfer, S. Sadaf, L. Walder, K. Kuepper, S. Dinklage, J. Wollschläger, L. Schneider, M. Steinhart, J. Hardege and D. Daum, *Energy Environ. Sci.*, 2015, **8**, 2685–2697.
38 L. D. Burke and E. J. M. O'Sullivan, *J. Electroanal. Chem. Interfacial Electrochem.*, 1981, **117**, 155–160.
39 D. Thierry, D. Persson, C. Leygraf, N. Boucherit and A. Hugot-le Goff, *Corros. Sci.*, 1991, **32**, 273–284.
40 C. Johnston, *Vib. Spectrosc.*, 1990, **1**, 87–96.
41 J. E. Maslar, W. S. Hurst, W. J. Bowers, J. H. Hendricks and M. I. Aquino, *J. Electrochem. Soc.*, 2000, **147**, 2532–2542.
42 J. Desilvestro, D. A. Corrigan and M. J. Weaver, *J. Electrochem. Soc.*, 1988, **135**, 885–892.
43 M. Vidotti, R. P. Salvador and S. I. Córdoba de Torresi, *Ultrason. Sonochem.*, 2009, **16**, 35–40.
44 C. Mockenhaupt, T. Zeiske and H. D. Lutz, *J. Mol. Struct.*, 1998, **443**, 191–196.
45 J. Yang, H. Liu, W. N. Martens and R. L. Frost, *J. Phys. Chem. C*, 2010, **114**, 111–119.
46 D. S. Hall, D. J. Lockwood, C. Bock and B. R. MacDougall, *Proc. R. Soc. A*, 2015, **471**, 20140792.
47 H. B. Li, M. H. Yu, F. X. Wang, P. Liu, Y. Liang, J. Xiao, C. X. Wang, Y. X. Tong and G. W. Yang, *Nat. Commun.*, 2013, **4**, 1894.
48 A. P. Grosvenor, B. A. Kobe, M. C. Biesinger and N. S. McIntyre, *Surf. Interface Anal.*, 2004, **36**, 1564–1574.
49 J. Y. C. Chen, L. Dang, H. Liang, W. Bi, J. B. Gerken, S. Jin, E. E. Alp and S. S. Stahl, *J. Am. Chem. Soc.*, 2015, **137**, 15090–15093.
50 R. S. McEwen, *J. Phys. Chem.*, 1971, **75**, 1782–1789.
51 C. Tessier, P. H. Haumesser, P. Bernard and C. Delmas, *J. Electrochem. Soc.*, 1999, **146**, 2059–2067.
52 R. D. L. Smith, M. S. Prévot, R. D. Fagan, Z. Zhang, P. A. Sedach, M. K. J. Siu, S. Trudel and C. P. Berlinguette, *Science*, 2013, **340**, 60–63.
53 M. Gong and H. Dai, *Nano Res.*, 2014, **8**, 23–39.
54 X. Lu and C. Zhao, *Nat. Commun.*, 2015, **6**, 6616.
55 Y. Lee, J. Suntivich, K. J. May, E. E. Perry and Y. Shao-Horn, *J. Phys. Chem. Lett.*, 2012, **3**, 399–404.
56 D. A. Corrigan, R. S. Conell, C. A. Fierro and D. A. Scherson, *J. Phys. Chem.*, 1987, **91**, 5009–5011.
57 M. P. Browne, S. Stafford, M. O'Brien, H. Nolan, N. C. Berner, G. S. Duesberg, P. E. Colavita and M. E. G. Lyons, *J. Mater. Chem. A*, 2016, **4**, 11397–11407.